



HAL
open science

Mechanical response of carbon paper Gas Diffusion Layer under patterned compression

Tristan Le Carre, Jean-François Blachot, Jean-Philippe Poirot-Crouvezier,
Jerome Laurencin

► To cite this version:

Tristan Le Carre, Jean-François Blachot, Jean-Philippe Poirot-Crouvezier, Jerome Laurencin. Mechanical response of carbon paper Gas Diffusion Layer under patterned compression. International Journal of Hydrogen Energy, 2023, pp.10.1016/j.ijhydene.2023.08.104. 10.1016/j.ijhydene.2023.08.104 . cea-04208417

HAL Id: cea-04208417

<https://cea.hal.science/cea-04208417>

Submitted on 15 Sep 2023

HAL is a multi-disciplinary open access archive for the deposit and dissemination of scientific research documents, whether they are published or not. The documents may come from teaching and research institutions in France or abroad, or from public or private research centers.

L'archive ouverte pluridisciplinaire **HAL**, est destinée au dépôt et à la diffusion de documents scientifiques de niveau recherche, publiés ou non, émanant des établissements d'enseignement et de recherche français ou étrangers, des laboratoires publics ou privés.



Distributed under a Creative Commons Attribution - NoDerivatives 4.0 International License

Mechanical Response of Carbon Paper Gas Diffusion Layer Under Patterned Compression

Tristan LE CARRE¹, Jean-François BLACHOT^{1,*}, Jean-Philippe POIROT-CROUVEZIER¹, Jérôme LAURENCIN²

¹Univ. Grenoble Alpes, CEA, Liten, DEHT, 38000 Grenoble, France

²Univ. Grenoble Alpes, CEA, Liten, DTCH, 38000 Grenoble, France

*Corresponding author: jean-françois.blachot@cea.fr, 17 avenue des Martyrs 38054 Grenoble Cedex, France; T.+33 4 38 78 14 82

Accepted manuscript – International Journal of Hydrogen Energy

DOI : [10.1016/j.ijhydene.2023.08.104](https://doi.org/10.1016/j.ijhydene.2023.08.104)

Abstract

The Proton Exchange Membrane Fuel Cell (PEMFC) performances are strongly impacted by the compression of the Gas Diffusion Layer (GDL). Despite its fibrous microstructure, this material is usually considered as a continuous medium and characterized with uniform loading. However, the GDL is subjected to a heterogeneous compression onto rib/channel patterns in the fuel cell assembly. In the present study, a complex behavior of the GDL response is experimentally revealed when the material is loaded with a rib/channel pattern, compared to uniform compression. The tests are simulated by finite element modeling using a classical strain-dependent elastic law, using parameters fitted from uniform compression experiments. It is shown that the numerical results do not reproduce the effect of pattern observed experimentally. Hypotheses to interpret these results involve mechanisms at the fiber microscale including fiber fracture, cross-link breakage and fiber rearrangement, which are exacerbated by larger material deformation caused by the heterogeneous loading.

Keywords

Proton Exchange Membrane Fuel Cell, Gas Diffusion Layer, Heterogeneous compression, Rib/channel pattern, Fiber microstructure, Finite Element Modeling

1. Introduction

Proton Exchange Membrane Fuel Cells (PEMFCs) are considered as a very promising solution to replace the combustion engine for transport applications. Indeed, the PEMFCs have received a growing interest in the recent years, as they offer high efficiency without carbon emission in operation [1,2].

A typical PEMFC is a multilayered assembly composed of a membrane and catalyst layers, associated with two Gas Diffusion Layers (GDLs) and flow field plates. Among the major components, the GDL ensures several functions as it should (i) distribute homogeneously the reactants from the flow field channels to the catalyst layers where the electrochemical reactions take place, (ii) collect the current and conduct the heat from the catalyst layers to the flow field plates and extract the produced water, (iii) mechanically support the multilayer structure [3]. A typical GDL is composed of a sheet made of entangled carbon fibers bonded by adhering contacts and treated with Polytetrafluoroethylene (PTFE) used as hydrophobic agent [4,5]. The GDL can be coated on one of its surface by a microporous layer to improve the contact with



the catalyst layer and the water management. Three main categories of GDL materials have been reported in the literature, based on the fiber arrangement at the microscale, namely the carbon cloth and carbon paper with straight stretched fibers or felt/'spaghetti' fibers [6].

An overall compressive pressure is applied on the PEMFCs during assembly [3,7], inducing a mechanical loading for each of its components. It has been widely reported that the whole fuel cell performances can be strongly affected by the GDL compression [8–15]. Indeed, when the assembly is submitted to the clamping, there is a competition between two phenomena that can deteriorate or improve the cell operation. On the one hand, the gas transport in the GDL can be significantly hindered by the GDL densification under compression [15–18]. In addition, the GDL intrusion in the channels reduces the effective cross-section area and consequently blocks the reactants [19–21]. On the other hand, the bulk and interfacial conductivities can be enhanced by the compression [22–28].

Because of its significant influence on the overall stack performance, an increasing number of studies has been recently devoted to the GDL in order to elucidate its complex mechanical behavior. Due to its highly porous fibrous microstructure, the GDL exhibits a non-linear behavior when loaded under uniform compression [10,23,29–31]. It has been proposed that the nonlinearity of the macroscopic response could be explained by the apparition of new contact points between the fibers subjected to a bending under compression at the microscale [23,30,32]. Moreover, the GDL strain is not fully reversible and presents a residual deformation after loading [10,31,33,34].

A number of models have been already proposed in the literature to represent this original behavior. Some of them assume a linear elastic behavior with a strain-dependent Young modulus, for which the parameters were identified with a polynomial fit [23,30]. This type of model has been widely used for the simulation of the assembly compression, in order to investigate the GDL interaction with the flow field plates or its influence on current distribution [23,30,35–39]. Some other authors have proposed a material behavior based on the homogenization of the unit beam cell deformation at the microscale [32,40,41]. This model should be more representative of the physical processes occurring during material loading. However its implementation requires more input data, especially on the microstructural properties. Recently, Carral and Mélé used the fibrous material model developed by Van Wyk and Toll [42,43] to represent the compressive behavior of non-woven GDL, including its cyclic response [29,44].

In the aforementioned models, the GDL is considered as a continuous media associated with a homogeneous mechanical behavior. Nevertheless, in the fuel cell assembly, the GDL loading with the rib/channel patterns of the flow field plates induces highly heterogeneous deformations [45–47]. Moreover, some authors pointed out the interest of reducing the channel width under 1mm for improved performances [48–50]. In this condition, it can be suspected that the local multiaxial stress state in the GDL induced by the heterogeneous deformation could result in a heterogeneous behavior for the GDL due to its complex microstructure. Therefore, the simulations performed under the assumption of a continuous homogenous medium can be questionable, especially when the channel size is in the range of the microstructure characteristic length [51]. In this context, Xiao et al. have simulated a uniform and heterogeneous compression of the GDL at the fiber scale. For this purpose, they have applied a finite element code to investigate the local deformation modes and stress distribution in a randomly generated microstructure [52] and microstructures reconstructed by X-ray computed microtomography [53,54]. The GDL deformation under uniform compression was validated by quantifying morphological criteria (local porosity, pore size distribution) as well as transport properties, thermal and electrical conductivity [53]. However, the total applied force was not extracted from the simulations, preventing comparison with experimental characterizations carried out at the macroscale. Conversely, Zhang et al. have compared the simulated uniform

compression at the microscale with experimental data, but did not consider the heterogeneous loading [55].

Regarding the experimental studies, most of the investigations on the GDL deformation under the compression of rib/channel pattern have been focused on the GDL intrusion in the channel [19,21,45–47,56,57]. However, none of them has linked their results with the average response of the material considered as a continuous medium.

In this study, the GDL macroscopic response under heterogeneous compression by rib/channel pattern is investigated experimentally. A particular attention is paid to the result reproducibility, which is challenging because of the inherent material dispersion. The effect of rib and channel width is discussed, focusing on the case of thin patterns (widths from 200 to 600 μm) representative of state-of-the-art or under development designs [48]. A complex behavior is highlighted from the experimental results, with a strong difference arising between heterogeneous and uniform compression. Moreover, a material model based on a polynomial fitting of experimental data from uniform compression is used to simulate the GDL compression under the same pattern lengths. The numerical results are compared with experimental data, in order to discuss the model ability to reproduce the experimental response.

2. Material and method

2.1. Experimental set-up

A typical commercial GDL provided by SGL Carbon (Sigracet 22BB) was considered for this study. It is a straight fibers carbon paper, PTFE impregnated and coated with a microporous layer. The total thickness given by the manufacturer is $215 \pm 15 \mu\text{m}$ [5,58].

In the PEMFC assembly, the GDL is located between the flow field plates and the membrane. As illustrated in Figure 1a, the standard case of identical anodic and cathodic ribs placed face to face was considered for the present study. It was also assumed that the membrane does not play a role on the mechanical response of the assembly loaded under compression. Indeed, the thickness of state-of-the-art membrane is under $15\mu\text{m}$ [59], which can be considered fully negligible compared to the other components. Moreover, the GDL exhibits a high compressibility, so it controls the assembly deformation. Therefore, taking advantage of the symmetry of the considered geometry, the compression of the GDL between rib channel patterns and a flat plate was chosen as a representative loading case.

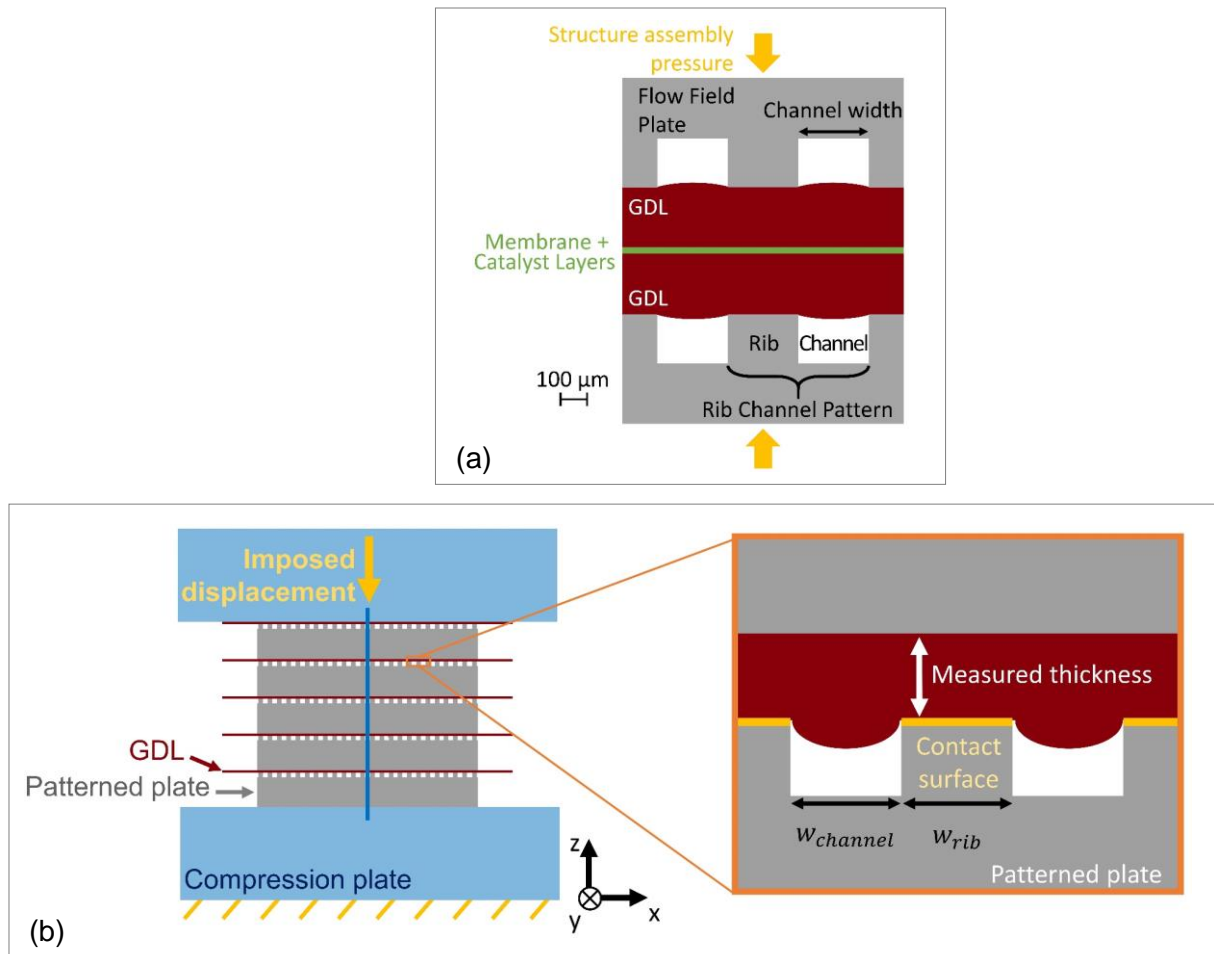


Figure 1 - (a) Schematic representation of a PEMFC structure, and (b) experimental set-up, with a zoom on local deformation.

The experimental set-up consists in a stack of five GDL samples separated with metal plates. As shown in Figure 1b, each plate is manufactured with a flat surface on one side, and an array of straight rib/channel patterns homogeneously distributed on the other side. Each GDL sample is compressed between a rib/channel pattern and a flat surface at the back of the next pattern. The choice of this configuration composed of several repeat units allows increasing the magnitude of the measured displacement and averaging the material response, in order to reduce the relative error. The centering of the five elements for the compression is ensured with a metallic needle (diameter 1mm) adjusted to the test machine plates, and getting through the stack, which is pierced in its middle (diameter 1.1mm) (Note the needle is represented by the blue line in Figure 1b). The contact between the needle and the elements of the stack is assumed frictionless, so its impact on the results could be neglected. The GDL samples are cut at a dimension larger than the patterned plates. Previous experiments have shown that, in this condition, edge effects could be considered negligible.

The experiments are conducted with a 3R SYNTAX 100kN machine. One compression step is applied at controlled displacement speed of 0.5 mm/min, corresponding to a strain rate of $6.2 \cdot 10^{-3} \text{ s}^{-1}$, to reach the targeted stress of 5 MPa. Calibration tests are realized by pressing the stack of patterned plates without GDL samples in order to remove its deformation. The total thickness of the five-sample stack and the total applied force are measured during the experiments with a 10Hz frequency. Therefore, the GDL thickness t_m deduced from the measurements corresponds to the spacing between the rib and the adjacent plate (see focus on Figure 1b). Additionally, the average pressure p_a is calculated with respect to the total

surface of one plate rather than the contact surface under the ribs. This choice allows an immediate comparison with the data commonly reported for the PEMFC application [9,12,15].

For the post-treatment analysis, two additional physical quantities are introduced. The average stiffness is defined as $K_a = \partial p_a / \partial t_m$, representing the apparent stiffness of the GDL under patterned compression. Moreover, mechanical response of fibrous material is often represented as a function of relative density [29,42–44]. In the present study, this quantity cannot be directly measured, as the heterogeneous compression induces disparities of relative density in the GDL. Nevertheless, its value under the ribs has been assessed as a function of the measured thickness using the following equation [29,44]:

$$\rho_m = \frac{A_w}{\rho_f t_m}, \quad (1)$$

where A_w is the sample areal weight and ρ_f is the fiber density, assumed to be equal to 1.8 g/cm^3 [4].

The impact of the pattern length on the compression behavior is analyzed using several dimensions of rib and channel for the manufactured plates, as reported in Table 1. In the following, the pattern configuration is named as “ $w_{rib}/w_{channel}$ pattern”, with width given in μm . Moreover, the ratio of channel width over rib width is denoted by $r_w = w_{channel}/w_{rib}$. A reference test is performed using a flat plate, to have a comparison with the case of uniform compression.

Table 1 - Pattern length list.

w_{rib} μm	$w_{channel}$ μm	r_w -
200	200	1
300	300	1
400	400	1
500	500	1
100	200	2
200	400	2
300	600	2

For the post-test characterizations, the GDL sample surface is observed using a digital microscope Olympus DSX1000. In addition, the tested samples are also characterized using a Scanning Electron Microscope (SEM) Leo 1530 from Zeiss (Oberkochen, Germany). Images are acquired in Secondary Electron (SE) mode with an accelerating voltage of 10 kV and a working distance of 7.8 mm.

2.2. Numerical model

The state-of-the art model based on the work of Kleeman et al. [23] which has been developed to account for the nonlinearity of the GDL compressive behavior, has been widely used in the literature [23,30,35,37,39]. It was shown that this model is able to reproduce correctly the uniform compression tests. This model assumes an orthotropic linear elastic behavior, with a strain-dependent Young modulus $E_z(\varepsilon_{zz})$ accounting for the compressive nonlinearity in the direction out of the material plane (z on Figure 2). The 2-dimension formulation of this model could be written as follows:

$$\begin{bmatrix} \sigma_{xx} \\ \sigma_{zz} \\ \sigma_{xz} \end{bmatrix} = \begin{bmatrix} \frac{E_x}{1 - \nu_{xz}^2} & \frac{\nu_{xz} E_x}{1 - \nu_{xz}^2} & 0 \\ \frac{\nu_{xz} E_z(\varepsilon_{zz})}{1 - \nu_{xz}^2} & \frac{E_z(\varepsilon_{zz})}{1 - \nu_{xz}^2} & 0 \\ 0 & 0 & G_{xz} \end{bmatrix} \cdot \begin{bmatrix} \varepsilon_{xx} \\ \varepsilon_{zz} \\ 2\varepsilon_{xz} \end{bmatrix} \quad (2)$$

In this equation, σ_{ij} and ε_{ij} refer to the components of the Second Piola Kirchhoff tensor and the Green-Lagrange strain tensor respectively. The stiffness matrix components are expressed using the Young's (E_x , E_z) and shear moduli (G_{xz}) and Poisson ratio (ν_{xz}).

In the present study, in order to assess the ability of Kleeman's model to reproduce the GDL heterogeneous compression, the test has been simulated using finite element method. In this objective, the Kleeman's model has been implemented into COMSOL Multiphysics 6.0 software using the Structural mechanics module [60]. The Poisson ratio out of the GDL plane is usually considered to be $\nu_{xz} = 0$ due to the highly porous structure [23]. The out-of-plane Young modulus E_z was identified from the uniform compression test with a polynomial fit of the secant Young modulus, defined as $E_z = \sigma_{zz}/\varepsilon_{zz}$. The consistency of the implemented model with experimental data was verified thanks to the simulation of uniform compression test (section 3.3). The in-plane Young modulus was measured experimentally and set to $E_x = 1.2$ GPa. Nevertheless, it is worth noting that the simulation results are independent on this parameter, because of the null Poisson ratio. Finally, the shear modulus G_{xz} was not measured experimentally, because of the complexity to induce a pure shear sollicitation in the material. A sensitivity analysis showed that this parameter choice did not significantly affect the simulation results and their interpretations. For the simulations, the shear modulus was set to $G_{xz} = 5$ MPa, which is the order of magnitude of the data reported a similar GDL from the same manufacturer [61]. All the properties used for the simulations are listed in Table 2.

The Figure 2 shows the simulated domain. The computations are carried out in plane strain conditions while the geometry is restricted to a single rib/channel pattern. These simplifications can be considered relevant regarding the pattern periodicity and the straight channels, and assuming that the boundary effects are negligible. The initial GDL thickness is taken at $215 \mu\text{m}$ based on the manufacturer's datasheet [58]. A small fillet corner is added at the rib edge (Figure 2) in order to avoid numerical artifacts due to a sharp singular point. A sensitivity analysis showed that this radius only influences the local stress profile in the GDL below the rib edge, without changing the global results and their interpretations.

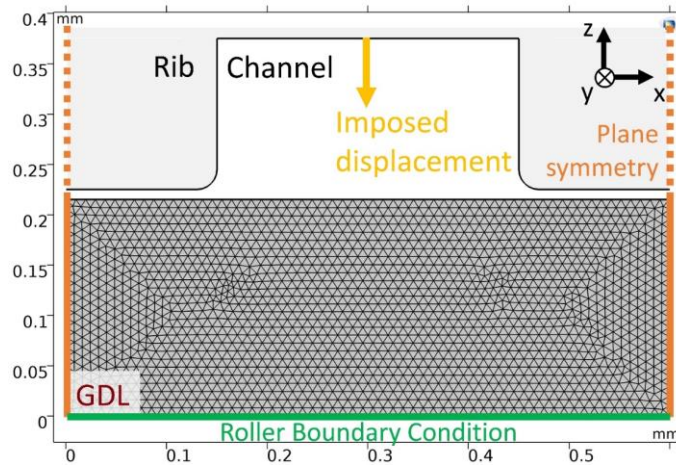


Figure 2 - Finite element model (300 μm /300 μm pattern).

The loading under compression is applied via the displacement of a rigid rib/channel indenter on the upper surface of the GDL (Figure 2). The contact is assumed frictionless. The maximum displacement is set to 100 μ m. Plane symmetry conditions are imposed on lateral surfaces, while a roller boundary condition is set on the lower surface. The geometric nonlinearity is considered in the simulation, because of the displacement amplitude and the contact.

A triangular mesh is imposed, with a 10 μ m characteristic size. Several automatic remeshing are used in the simulation in order to help for the convergence around the rib edge. Because of the high stress concentration below the rib edge, a time-dependent study is used with a quasi-static loading speed, identical to the experimental test. The absence of kinetic effect is verified before the post-treatment.

Finally, the exported variables are chosen for a direct comparison with experimental results: (i) the thickness t_m under the ribs, related to the indenter displacement, and (ii) the z component of the total reaction force on the GDL lower surface, equal to the average pressure when divided by the pattern width. The average stiffness and relative density are derived from average pressure and measured thickness using the same equations as for experimental data (described in section 2.1). Moreover, the pressure profile along this lower surface and the displacement profile on the upper GDL surface are also studied for the discussion and interpretation.

Table 2 – Material model parameters – Sigracet SGL 22BB.

Parameter	Value	
E_x	MPa	1200
$E_z(\epsilon_{zz})$	MPa	$1048.3 \epsilon_z^5 + 3338 \epsilon_z^4 - 1697.7 \epsilon_z^3 + 250.35 \epsilon_z^2 + 42.647 \epsilon_z + 2$
ν_{xz}	-	0
G_{xz}	MPa	5

3. Results

3.1. Experimental reproducibility

Due to their fibrous microstructure and manufacturing process, GDL materials show inherent disparities between samples (e.g. areal weight of the SGL 22BB reference is defined with a 21.4% error in the manufacturer datasheet [58]). Therefore, this section deals with the reproducibility of the results, in order to ensure the relevance of their forthcoming interpretations. For this purpose, three repetitions of the compression test were conducted for each pattern length. Figure 3 presents the results for 300 μ m/300 μ m pattern, which are representative of the phenomena observed for each pattern length.

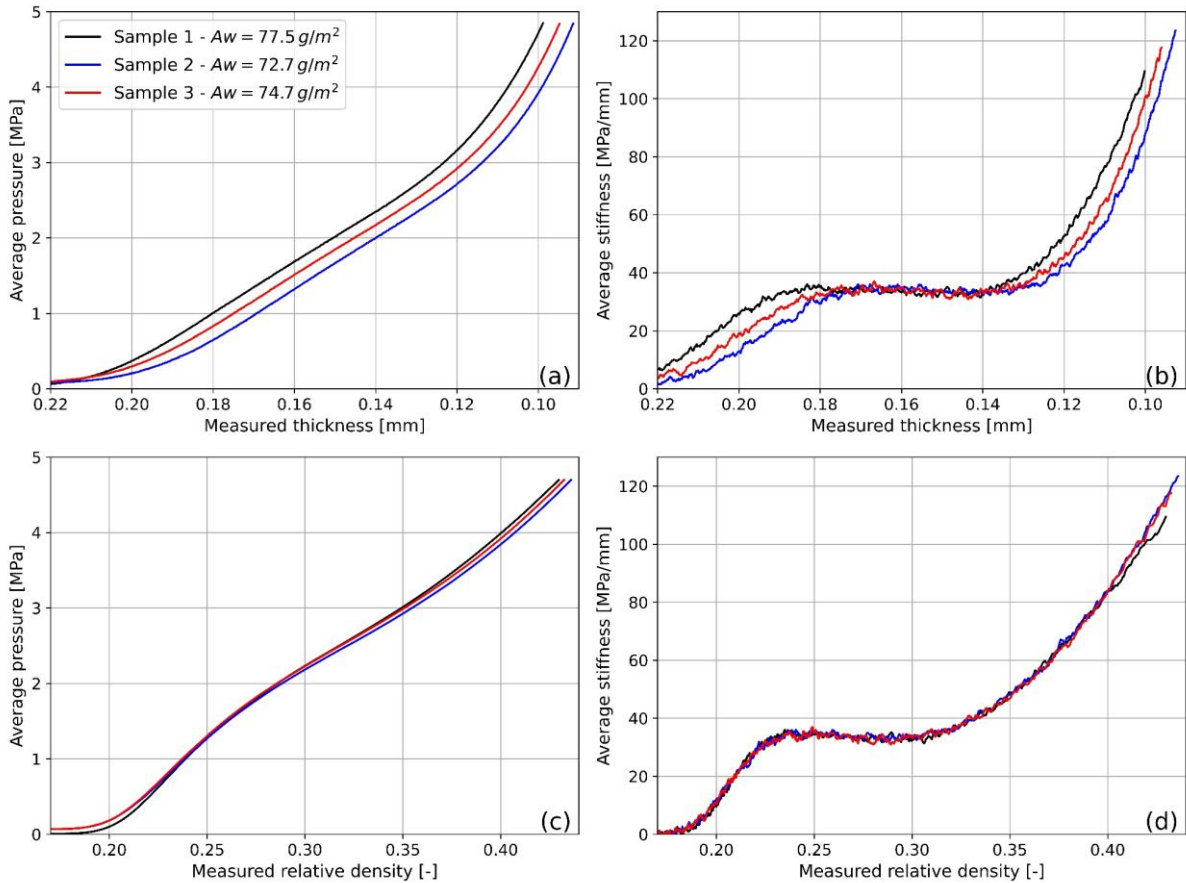


Figure 3 – Four different plots to present experimental reproducibility for three stacks compressed by $300\mu\text{m}/300\mu\text{m}$ pattern. In the insert of Figure 3a, the term A_w stands for the average areal weight of the stack samples.

As illustrated in Figure 3a, a noticeable but limited difference is observed for the average pressure plotted as a function of the measured thickness. However, it is worth noting that the slope of these curves, which corresponds to the average stiffness, is roughly similar for the three measurements. Therefore, this parameter appears as a good indicator to illustrate the test repeatability. It is plotted as a function of (i) the measured thickness and (ii) the measured relative density in Figure 3b and Figure 3d, respectively. While the average stiffness versus the thickness presents a shift between the three samples (Figure 3b), it appears that the representations using the relative density (Figure 3d) are almost superimposed. Thus, the offset observed in Figure 3b may correspond to a scattering on the initial sample thicknesses and should not reflect a difference in material properties between the tested samples (which seems to be good in our tested samples regarding Figure 3d). Therefore, the plot of the average stiffness versus the relative density is assumed to be correlated specifically to the interaction between the patterned indenter and the GDL.

The measurement of sample areal weight supports the interpretation that a scattering on the sample geometry induces the differences in Figure 3a and Figure 3b. Indeed, heavier samples resulted in a higher measured thickness. Since the use of relative density on x-axis essentially corresponds to an expression of the quantity of material, the absence of offset on this representation is coherent with previous observations (Figure 3d). Similarly, the representation

of the average pressure with respect to relative density (Figure 3c) also erases the disparities between samples.

In the following, the average pressure vs measured thickness and the average stiffness vs measured relative density are selected to represent the results. The former is used despite the offset observed between test repetitions, since it is the closest to the classical mechanical representation of stress versus strain evolution. The latter gives the evolution of average stiffness without the effect of material scattering.

3.2. Experimental observation of the effect of rib/channel pattern size

The experimental evolutions of the average pressure with the thickness and the average stiffness with relative density are displayed in Figure 4 for different patterns exhibiting a ratio of channel width over rib width of $r_w = 1$. The same plots are given in Figure 5 for a ratio of $r_w = 2$. The reference curve corresponds to the uniform compression by a flat plate and it is plotted in black on both figures. Considering the comments on reproducibility in section 3.1, a single measurement taken for the three tests is used for each pattern width.

First, the average pressure required to reach the same thickness is much lower for heterogeneous compressions than for the reference.

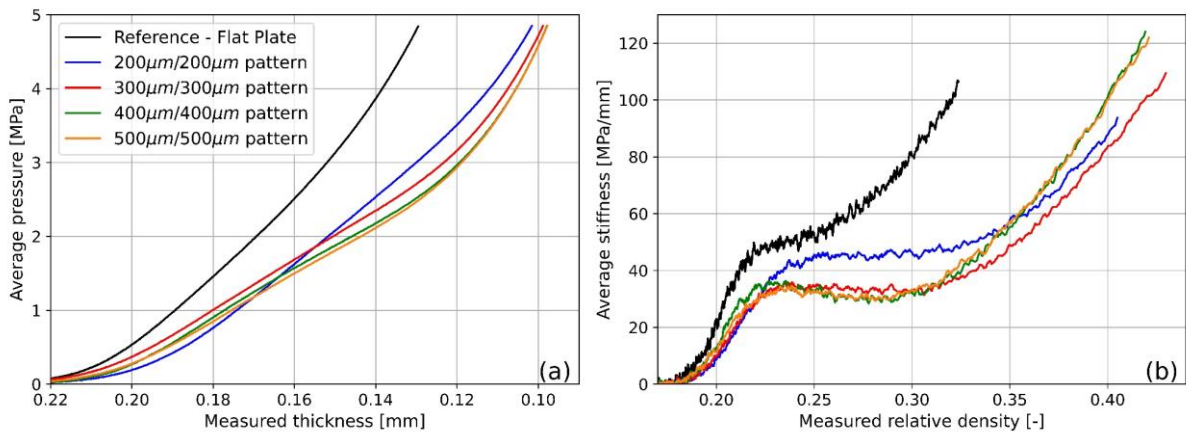


Figure 4 – Experimental effect of rib/channel pattern length on average pressure (a) and average stiffness (b) for $r_w = 1$.

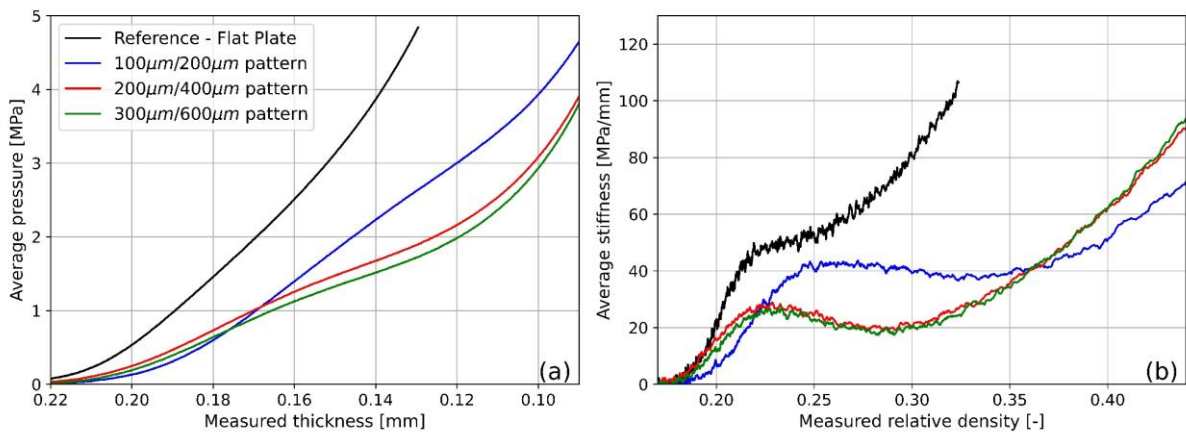


Figure 5 – Experimental effect of rib/channel pattern length on average pressure (a) and average stiffness (b) for $r_w = 2$.

For each pattern, it can be observed that the GDL compression behavior becomes highly nonlinear compared to the homogenous case. The material stiffness under uniform compression is monotonic. In contrast, for the channels larger than 300 μm , the heterogeneous compression presents two inflections of the average pressure vs measured thickness curve (Figure 4a and Figure 5a). These inflections correspond to extrema of the derivative curve, i.e. the average stiffness (Figure 4b and Figure 5b). These effects intensify with the pattern size as they are more pronounced for $r_w = 2$. However, these inflections are not observed for 200 μm /200 μm pattern, while they are limited for the 100 μm /200 μm pattern.

3.3. Simulation results

The Figure 6 and Figure 7 present the simulated response of the GDL subjected to heterogeneous compressions, obtained with the model described in section 2.2. For channel widths larger than 300 μm , it can be noticed that problems of convergence stopped the simulation before the last calculation step. Nonetheless, calculated increments reach pressures higher than 2MPa, so that the computed interval includes the pressure commonly applied in the PEMFC assembly (around 1MPa). Thus, it is worth to compare these results to experimental curves.

In Figure 8, the simulated and experimental data are compared for the GDL loaded under uniform and heterogeneous compression (200 μm /400 μm , 400 μm /400 μm). As mentioned in section 2.2 for the homogeneous case, the simulation reproduces accurately the experimental data. Only a slight offset can be noted between the measured and computed thicknesses in Figure 8a. This deviation of the model from the experiments is probably due to a scattering in the material properties (commented in section 3.1). However, it is worth underlining that the evolution of the stiffness as a function of the relative density is perfectly predicted by the model (Figure 8b).

As expected, for both $r_w = 1$ and $r_w = 2$, the increase of the pattern size leads to lower assembly stiffnesses, resulting in a lower pressure at the same thickness under the ribs. This observation is consistent with experimental results before the second inflection. However, it is worth underlining that none of the simulations under heterogeneous compression reproduces the inflections observed experimentally (Figure 8). In other words, the standard model used for simulating the GDL behavior fails to simulate accurately the heterogeneous compressions.

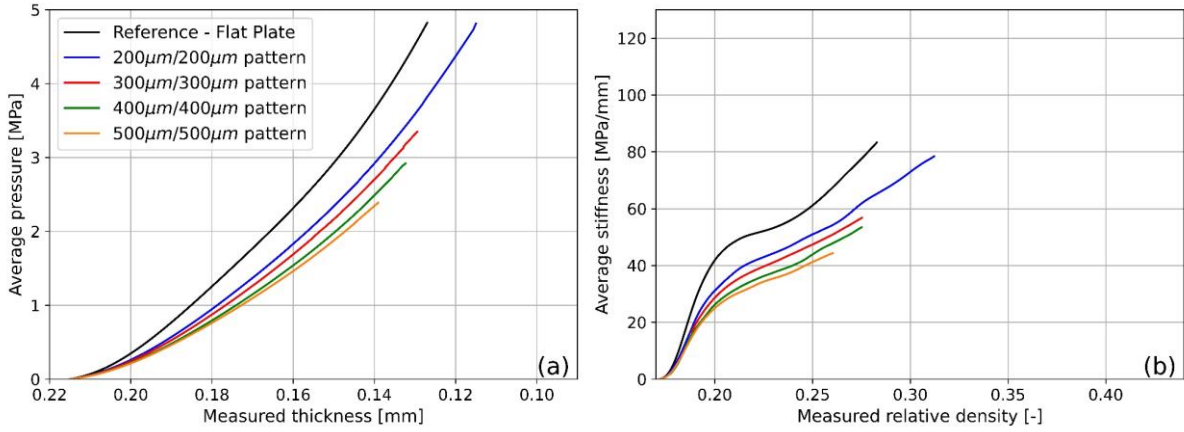


Figure 6 – Simulated average pressure (a) and average stiffness (b) for $r_w = 1$.

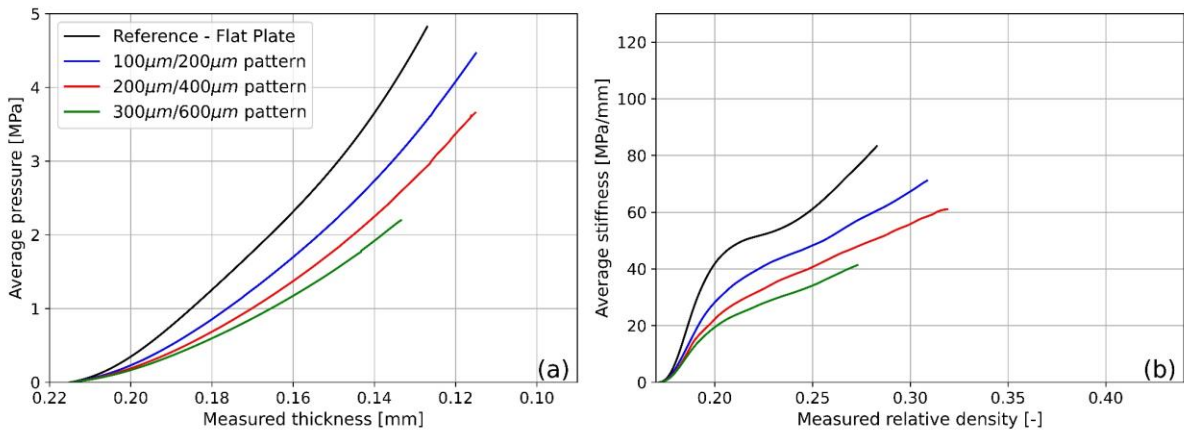


Figure 7 - Simulated average pressure (a) and average stiffness (b) for $r_w = 2$.

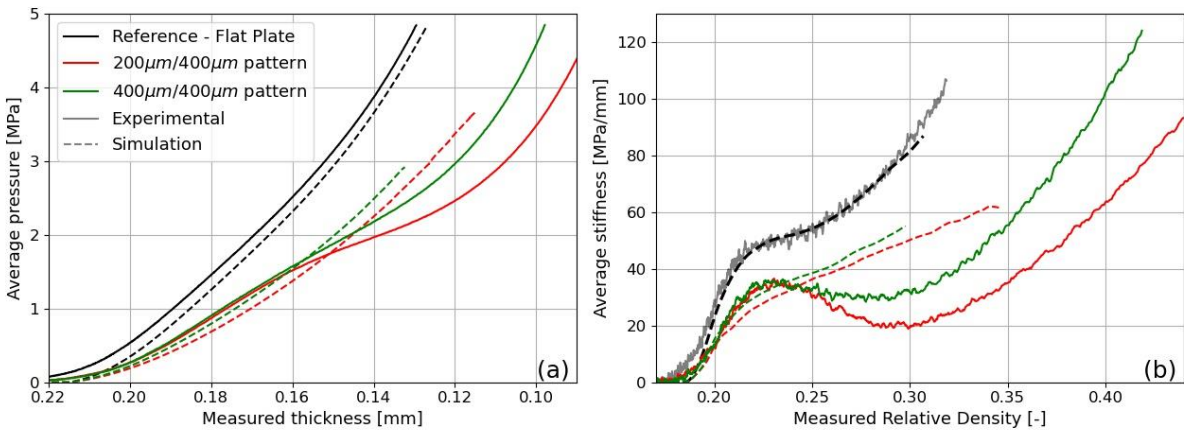


Figure 8 - Comparison of experiment (plain line) and simulation (dashed line) result for uniform compression and heterogeneous compression (200 $\mu\text{m}/400\mu\text{m}$, 400 $\mu\text{m}/400\mu\text{m}$).

4. Discussion

This section first deals with the influence of the pattern width on the GDL mechanical response, and then draws some hypotheses to interpret the experimental results. Finally, the implications on PEMFC assembly are discussed.

4.1. Effect of the rib/channel pattern width

Two distinct trends seem to emerge from the experimental compression tests depending on the considered pattern length.

On the one hand, the GDL response for the thinnest channels (i.e. 200 μm) differs notably from the behavior obtained with larger pattern widths (Figure 4, Figure 5). Indeed, the results become similar to those recorded for a uniform compression, without the curve inflections. This pattern length may have induced a more homogeneous strain and stress repartition in the material, inducing a pressure-thickness evolution closer to the reference.

On the other hand, it seems that the material behavior can be controlled by the contact surface for larger patterns. Indeed, the difference between material responses tends to vanish when growing the pattern width. As illustrated for $r_w = 1$, a limit might have been reached between 300 $\mu\text{m}/300\mu\text{m}$ and 400 $\mu\text{m}/400\mu\text{m}$ patterns, resulting in a similar material response for 400 $\mu\text{m}/400\mu\text{m}$ and 500 $\mu\text{m}/500\mu\text{m}$ patterns (Figure 4). Likewise, the inflections of the compression curve under 200 $\mu\text{m}/400\mu\text{m}$ and 300 $\mu\text{m}/600\mu\text{m}$ patterns occurred at the same measured relative density (Figure 5).

Although the simulated compression test cannot reproduce accurately the complexity of the GDL response, the results can still be exploited to help the understanding of pattern width effect. Figure 9b and Figure 10b present the simulated pressure profile on the lower surface of the GDL, which is at the opposite surface of the patterned indenter, for an imposed displacement of 75 μm . The resulting compression ratio of the GDL is larger than the usual value in fuel cell assembly, however it is especially relevant for the present mechanical study, as the pattern length effects should be emphasized under larger deformation. For the ribs above 300 μm , the pressure under the ribs reaches the same value whatever the pattern. This is a consequence of the null Poisson ratio, causing a pure uniform compression under the land, with no influence of the material behavior located under the channels. However, below 300 μm , the simulated stress under the ribs decreases with decreasing the rib size (from 3.5 MPa down to 3.1 MPa when changing the rib size from 300 μm to 100 μm). In this case, the rib size becomes too small to reach the upper bound for the stress given by the uniform compression (i.e. the black line in Figure 9 related to the flat plate). Moreover, the pressure decreases under the channel, in larger proportions for larger channels. This observation agrees with the lower average pressure obtained for the same imposed displacement. However, it is worth reminding that these simulations are not able to reproduce the unexpected behavior highlighted in the experiments for heterogeneous compression. Since the model considered a homogeneous medium for the GDL, it can be reasonably proposed that the model's inadequacy could originate from the GDL fibrous microstructure.

In this frame, the scale effect observed for the thinnest patterns in the experiments (100 $\mu\text{m}/200\mu\text{m}$ and 200 $\mu\text{m}/200\mu\text{m}$) could be related to the material heterogeneity at the microscale. Indeed, the GDL mechanical behavior under compression is controlled by the fiber bending between contact points [41]. The characteristic length for the bending fiber in the microstructure is around 130 μm for a similar GDL provided by the same manufacturer (24AA, 25AA). Therefore, the assumption of a continuous medium for the GDL is even more

questionable for the thinnest patterns. In this case, the local heterogeneities in the GDL can strongly affect its overall mechanical response.

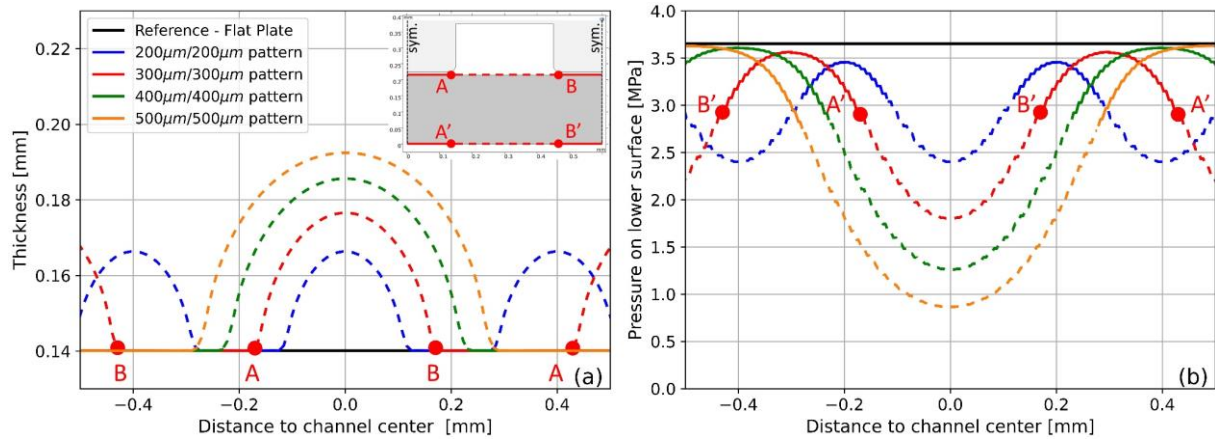


Figure 9 – GDL thickness profile (left) and pressure on the lower surface (right) under an imposed displacement of $75 \mu\text{m}$ for $r_w = 1$. Solid lines and dashed lines correspond to the region under the rib and the channel respectively. The insert on Figure 9a gives the position of rib/channel boundaries for the $300\mu\text{m}/300\mu\text{m}$ pattern.

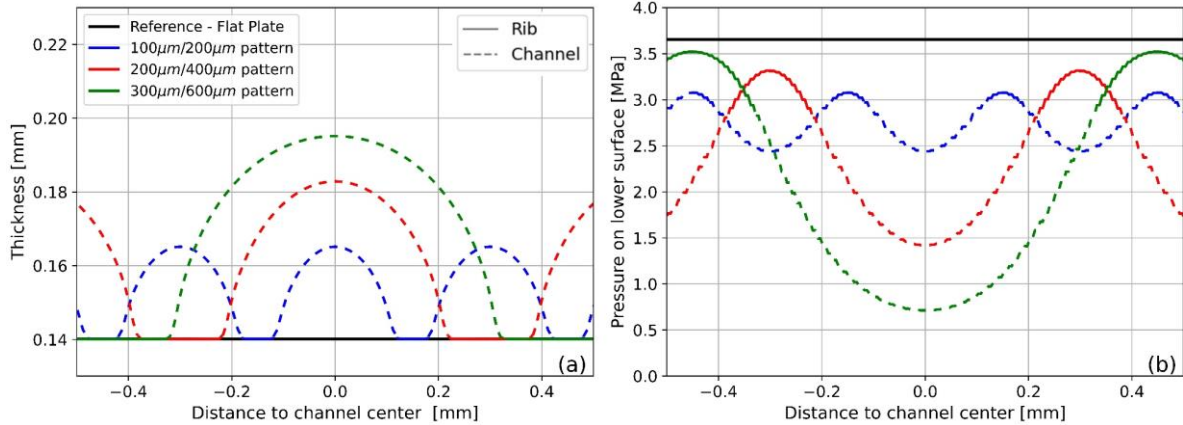


Figure 10 - GDL thickness profile (left) and pressure on the lower surface (right) under an imposed displacement of $75 \mu\text{m}$ for $r_w = 2$. Solid lines and dashed lines correspond to the region under the rib and the channel respectively.

4.2. Behavior of the fibrous structure of the GDL

As mentioned in section 1, the nonlinearity of the GDL behavior under uniform compression has been already widely discussed in the literature (reference curve on Figure 4a). The material hardening (i.e. increase in stiffness as shown in Figure 4b and Figure 5b) is often attributed to the increasing number of contact points between the fibers constituting the GDL during the compression [23,30,32]. The interval for which the hardening is lower (for a relative density from 0.22 to 0.25 on reference curve on Figure 4b and Figure 5b) can be still interpreted with the behavior of fiber bending. Indeed, in this region, much fewer new contact points are created leading to an almost linear behavior with constant stiffness [30,41]. Nonetheless, on the same stress interval, several authors observed a decreasing stiffness rather than a plateau,

resulting in inflections on the stress-strain curve, with various interpretations. Carral and Mélé [29,44] referred to the effect of a compression pressure applied during the manufacturing process which damages the material. Thus, it would cause a different material response at low stresses, while the “original behavior” would only be observable for stresses higher than the manufacturing compression pressure. Alternatively, Mezeix et al. [62] emphasized that cross links between the piled fibers are progressively broken during the compression test. The measured behavior presents inflections at low stresses, before an important material densification at higher stresses.

In contrast, the present results have highlighted an important effect of rib/channel pattern length on the GDL mechanical response. In particular, the numerical model takes into account the behavior nonlinearity but cannot reproduce inflections of the experimental response. Therefore, these effects could be due to a new phenomenon associated to an irreversible damage in the microstructure. On the other hand, we cannot exclude a different manifestation of the local nonlinearities when the GDL is subject to the triaxial stress state induced by the heterogeneous compression and not included in state-of-the-art material models.

Regarding the first hypothesis, an interpretation could be based on a damage localized around the edge of the rib, due to cross-link breakage and fiber fracture. Indeed, optical microscope observations of the GDL have revealed fiber fractures after the compression test (Figure 11). These fractures are located along parallel lines regularly spaced that must correspond to the rib edges. Indeed, the heterogeneous compression must induce a larger material distortion just below the rib edge line, accompanied with a shear stress hot spot. Yet, these stress concentrations occur independently of the pattern length. As illustrated in Figure 9a and Figure 10a, the numerical simulations have shown that the material distortion around the edge is similar whatever the channel length. Likewise, the fiber fractures were observed for each pattern size, even for the thinnest channel. Consequently, the stress concentration around the rib edge could not explain alone the effect of pattern length on the GDL response.

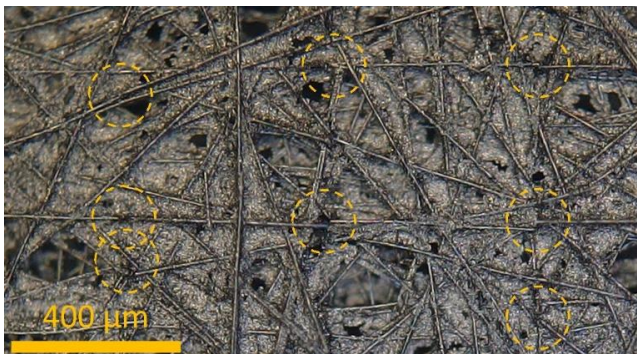


Figure 11 - Fiber fracture in a GDL submitted to 5MPa compression by 500μm/500μm pattern (digital microscope observation).

Another interpretation would be the influence of fiber rearrangement and damages in the GDL bulk rather than around the rib edge, such as cross-link breakage that has been observed in the literature on similar GDL materials [10,33]. These bonds can be ensured either by the binder incorporated during the papermaking process [5], or by the PTFE impregnated afterwards, which is mainly located at the fiber junctions [63,64]. The relevance of the last hypothesis is confirmed by SEM observations of GDL samples after mechanical loading. Indeed, as shown in Figure 12, several debondings of the PTFE between fibers are detected in the tested samples, while they are not observed in the pristine GDL. This fracture mechanism is linked to the stress level and thus may occur under the rib, similarly to uniform

compression, but also under the channel depending on the extent of stress propagation. Moreover, the deformation heterogeneities in the material also causes a region of higher fiber rotation and bending, mainly located in GDL thickness under the rib edge. This deformation mode does not happen under uniform compression, and it might intensify cross-link breakage and fiber rearrangement. Consequently, the distance between neighboring ribs could explain the pattern length effect, with higher deformation heterogeneity for larger channels.

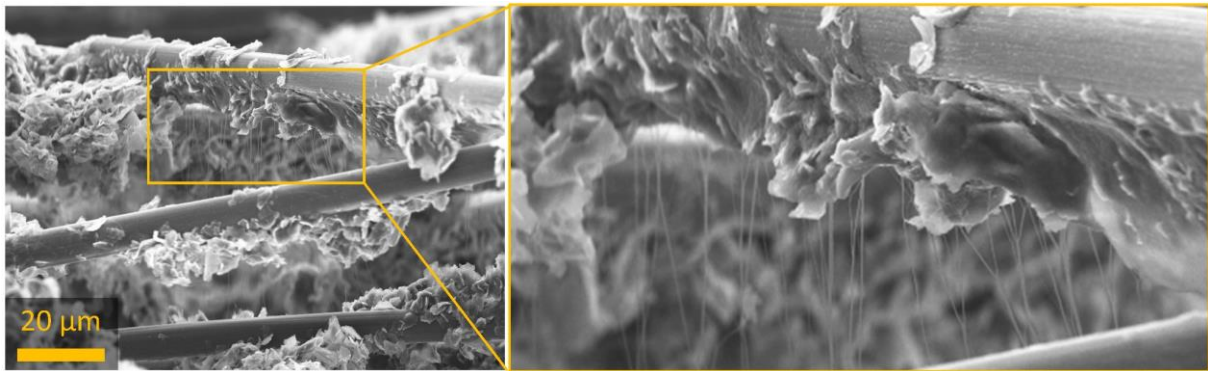


Figure 12 – SEM image of PTFE debonding in a GDL submitted to 5MPa compression by 400µm/400µm pattern.

The latter hypothesis is consistent with the numerical model inability to reproduce the experimental response. On the one hand, the microstructural mechanisms may be well represented by the strain-dependent Young modulus in the GDL region located under the land, as the solicitation corresponded to the uniaxial compression used for the modeling. On the other hand, the complex deformation under the rib edge is not taken into account in the model, so it could not represent any change of microstructural mechanisms, such as additional cross-link breakages. A model improvement might be the consideration of other parameters in the out-of-plane Young modulus definition, such as shear strain. Moreover, other material characteristics than the Young modulus may not be constant, such as the out-of-plane shear modulus or the Poisson ratio, already mentioned by Afrasiab et al. [65].

4.3. Implications on PEMFC assembly

The present study stresses out a gap between the material responses under heterogeneous compression by up-to-date rib/channel patterns compared to the uniform compression that is widely used for GDL characterization [23,30,35–39,66]. Actually, these differences in the deformation of the GDL are not taken into account in a PEMFC assembly, from the laboratory cell to the full stack scale, although the associated stress repartition and GDL intrusion cannot be considered as similar.

On the one hand, under a controlled average pressure of 1MPa [12], the GDL thickness under the ribs may be systematically overestimated, with a thickness under the ribs around 170 µm instead of 190 µm on Figure 5a for example. This lower thickness should induce a lower porosity for the GDL and deteriorate the transport properties [15–18].

On the other hand, under controlled GDL thickness with wedges or gaskets, the average pressure is overestimated in the case of patterned compression compared to the reference. Indeed, for an imposed GDL thickness under the ribs of 190 µm, the average pressure under patterned compression is lower than 0.5 MPa, instead of the targeted 1 MPa measured under

uniform compression. Therefore, the stress repartition in the assembly which controls notably the contact resistance is significantly affected.

Moreover, the GDL deformation impacts particularly its porosity and tortuosity and its intrusion in the channels, which values strongly influence the overall fuel cell performance [19,21]. Yet, the present study emphasized that a GDL numerical model based on classical characterization under uniform compression fails to predict correctly the material response under heterogeneous compression. Consequently, the gap between simulated and experimental deformation might modify significantly the prediction of pressure drop along channels and therefore decrease the precision of the multiphysic simulation that aims to predict performance from local rib/channel scale to overall stack scale [13,20,67,68].

Because of the aforementioned heterogeneities of deformation profile, transport properties and electric conductivity, the fuel cell presents current heterogeneities in operation [69–71]. These latter affect the ageing of several components, deteriorating the fuel cell durability [70,72]. Conversely, our results show that thinner patterns should result in lower heterogeneities and therefore may help for designing more durable fuel cell.

5. Conclusion and future works

The effect of heterogeneous compression of the GDL by rib/channel pattern has been studied. The experiments have revealed a complex behavior, which is not observed under uniform compression. Indeed, inflections have been highlighted in the curves of the applied pressure plotted as function of the GDL thickness only when the samples are loaded under heterogeneous compression. For channel widths larger than 300 μm , a threshold may have been reached with similar results for increasing pattern width above this limit. Conversely, thinner patterns result in a more homogeneous deformation with a behavior closer to the uniform compression.

The experiments have been simulated by finite element modeling using a strain-dependent out-of-plane Young modulus determined with the uniform compression test. It has been found that the simulations do not predict accurately the experimental response of the material under representative rib/channel patterns. In particular, the model does not reproduce the inflections observed experimentally. Therefore, the widely used strain-dependent elastic law is not suitable to simulate correctly the GDL response under heterogeneous loading.

Different hypotheses have been proposed to interpret the pattern effect, involving fiber rearrangement and damages at the microscale such as cross-link breakage or fiber fracture. These mechanisms might be enhanced by larger material deformation caused by the heterogeneous loading, and could explain the difference of the GDL response. To validate these assumptions, simulations of the heterogeneous loading of the GDL at the microscale are still necessary. In addition, the present study considered the symmetric case with anodic rib/channel pattern facing identical pattern on the cathodic side, which is a simplified structure compared to actual bipolar plate designs. This work could be extended by experiments to investigate the effect of different orientation or width on anodic and cathodic sides, or the effect of shifted patterns with channels facing ribs that would impose a shear loading of the GDL. These further investigations should allow a better understanding of the influence of the aforementioned local mechanisms in the GDL on the averaged material response.

References

- [1] Clean Hydrogen JU. Fuel Cells and Hydrogen Observatory. 2022.
- [2] Olabi AG, Wilberforce T, Abdelkareem MA. Fuel cell application in the automotive industry and future perspective. *Energy* 2021;214:118955. <https://doi.org/10.1016/j.energy.2020.118955>.
- [3] Khetabi EM, Bouziane K, Zamel N, François X, Meyer Y, Candusso D. Effects of mechanical compression on the performance of polymer electrolyte fuel cells and analysis through in-situ characterisation techniques - A review. *J Power Sources* 2019;424:8–26. <https://doi.org/10.1016/j.jpowsour.2019.03.071>.
- [4] Mathias MF, Roth J, Fleming J, Lehnert W. Diffusion media materials and characterisation. *Handb. Fuel Cells*, John Wiley & Sons, Ltd; 2010. <https://doi.org/10.1002/9780470974001.f303046>.
- [5] Schweiss R, Meiser C, Damjanovic T, Galbiati I, Haak N. SIGRACET® Gas Diffusion Layers for PEM Fuel Cells, Electrolyzers and Batteries (White Paper). SGL Fuel Cell Components; 2016.
- [6] El-kharouf A, Mason TJ, Brett DJL, Pollet BG. Ex-situ characterisation of gas diffusion layers for proton exchange membrane fuel cells. *J Power Sources* 2012;218:393–404. <https://doi.org/10.1016/j.jpowsour.2012.06.099>.
- [7] Millichamp J, Mason TJ, Neville TP, Rajalakshmi N, Jervis R, Shearing PR, et al. Mechanisms and effects of mechanical compression and dimensional change in polymer electrolyte fuel cells – A review. *J Power Sources* 2015;284:305–20. <https://doi.org/10.1016/j.jpowsour.2015.02.111>.
- [8] Atkinson RW, Garsany Y, Gould BD, Swider-Lyons KE, Zenyuk IV. The Role of Compressive Stress on Gas Diffusion Media Morphology and Fuel Cell Performance. *ACS Appl Energy Mater* 2018;1:191–201. <https://doi.org/10.1021/acsaem.7b00077>.
- [9] El-kharouf A, Steinberger-Wilckens R. The Effect of Clamping Pressure on Gas Diffusion Layer Performance in Polymer Electrolyte Fuel Cells. *Fuel Cells* 2015;15:802–12. <https://doi.org/10.1002/fuce.201500088>.
- [10] Escribano S, Blachot J-F, Ethève J, Morin A, Mosdale R. Characterization of PEMFCs gas diffusion layers properties. *J Power Sources* 2006;156:8–13. <https://doi.org/10.1016/j.jpowsour.2005.08.013>.
- [11] Ge J, Higier A, Liu H. Effect of gas diffusion layer compression on PEM fuel cell performance. *J Power Sources* 2006;159:922–7. <https://doi.org/10.1016/j.jpowsour.2005.11.069>.
- [12] Imscher P, Qui D, Janßen H, Lehnert W, Stolten D. Impact of gas diffusion layer mechanics on PEM fuel cell performance. *Int J Hydrog Energy* 2019;44:23406–15. <https://doi.org/10.1016/j.ijhydene.2019.07.047>.

- [13] Kulkarni N, Cho JIS, Jervis R, Roberts EPL, Francesco I, Kok MDR, et al. The effect of non-uniform compression on the performance of polymer electrolyte fuel cells. *J Power Sources* 2022;521:230973. <https://doi.org/10.1016/j.jpowsour.2021.230973>.
- [14] Lee W, Ho C-H, Van Zee JW, Murthy M. The effects of compression and gas diffusion layers on the performance of a PEM fuel cell. *J Power Sources* 1999;84:45–51. [https://doi.org/10.1016/S0378-7753\(99\)00298-0](https://doi.org/10.1016/S0378-7753(99)00298-0).
- [15] Mason TJ, Millichamp J, Shearing PR, Brett DJL. A study of the effect of compression on the performance of polymer electrolyte fuel cells using electrochemical impedance spectroscopy and dimensional change analysis. *Int J Hydrog Energy* 2013;38:7414–22. <https://doi.org/10.1016/j.ijhydene.2013.04.021>.
- [16] James JP, Choi H-W, Pharoah JG. X-ray computed tomography reconstruction and analysis of polymer electrolyte membrane fuel cell porous transport layers. *Int J Hydrog Energy* 2012;37:18216–30. <https://doi.org/10.1016/j.ijhydene.2012.08.077>.
- [17] Kulkarni N, Cho JIS, Rasha L, Owen RE, Wu Y, Ziesche R, et al. Effect of cell compression on the water dynamics of a polymer electrolyte fuel cell using in-plane and through-plane in-operando neutron radiography. *J Power Sources* 2019;439. <https://doi.org/10.1016/j.jpowsour.2019.227074>.
- [18] Zhu L, Zhang H, Xiao L, Bazylak A, Gao X, Sui P-C. Pore-scale modeling of gas diffusion layers: Effects of compression on transport properties. *J Power Sources* 2021;496:229822. <https://doi.org/10.1016/j.jpowsour.2021.229822>.
- [19] Keller N, Hübner P, von Unwerth T. Investigation of intrusion effects of a gas diffusion layer into channel cross sections depending on channel parameters of metallic bipolar plates. *Int J Hydrog Energy* 2020;45:15366–79. <https://doi.org/10.1016/j.ijhydene.2020.03.245>.
- [20] Kim A-R, Jung H-M, Um S. An engineering approach to optimal metallic bipolar plate designs reflecting gas diffusion layer compression effects. *Energy* 2014;66:50–5. <https://doi.org/10.1016/j.energy.2013.08.009>.
- [21] Lai Y-H, Rapaport PA, Ji C, Kumar V. Channel intrusion of gas diffusion media and the effect on fuel cell performance. *J Power Sources* 2008;184:120–8. <https://doi.org/10.1016/j.jpowsour.2007.12.065>.
- [22] El Oualid S, Lachat R, Candusso D, Meyer Y. Characterization process to measure the electrical contact resistance of Gas Diffusion Layers under mechanical static compressive loads. *Int J Hydrog Energy* 2017;42:23920–31. <https://doi.org/10.1016/j.ijhydene.2017.03.130>.
- [23] Kleemann J, Finsterwalder F, Tillmetz W. Characterisation of mechanical behaviour and coupled electrical properties of polymer electrolyte membrane fuel cell gas diffusion layers. *J Power Sources* 2009;190:92–102. <https://doi.org/10.1016/j.jpowsour.2008.09.026>.

- [24] Nitta I, Himanen O, Mikkola M. Contact resistance between gas diffusion layer and catalyst layer of PEM fuel cell. *Electrochem Commun* 2008;10:47–51. <https://doi.org/10.1016/j.elecom.2007.10.029>.
- [25] Shinde U, Koorata PK. A phase-dependent constitutive model to predict cyclic electrical conductivity in fuel cell gas diffusion media. *J Power Sources* 2022;527:231179. <https://doi.org/10.1016/j.jpowsour.2022.231179>.
- [26] Ye L, Qiu D, Peng L, Lai X. Microstructures and electrical conductivity properties of compressed gas diffusion layers using X-ray tomography. *Appl Energy* 2022;326:119934. <https://doi.org/10.1016/j.apenergy.2022.119934>.
- [27] Zhang L, Liu Y, Song H, Wang S, Zhou Y, Hu SJ. Estimation of contact resistance in proton exchange membrane fuel cells. *J Power Sources* 2006;162:1165–71. <https://doi.org/10.1016/j.jpowsour.2006.07.070>.
- [28] Zhang R, Yang B, Shao Z, Yang D, Ming P, Li B, et al. Graph theory model and mechanism analysis of carbon fiber paper conductivity in fuel cell based on physical structure. *J Power Sources* 2021;491:229546. <https://doi.org/10.1016/j.jpowsour.2021.229546>.
- [29] Carral C, Mele P. A constitutive law to predict the compression of gas diffusion layers. *Int J Hydrog Energy* 2018;43:19721–9. <https://doi.org/10.1016/j.ijhydene.2018.08.210>.
- [30] García-Salaberri PA, Vera M, Zaera R. Nonlinear orthotropic model of the inhomogeneous assembly compression of PEM fuel cell gas diffusion layers. *Int J Hydrog Energy* 2011;36:11856–70. <https://doi.org/10.1016/j.ijhydene.2011.05.152>.
- [31] Radhakrishnan V, Haridoss P. Effect of cyclic compression on structure and properties of a Gas Diffusion Layer used in PEM fuel cells. *Int J Hydrog Energy* 2010;35:11107–18. <https://doi.org/10.1016/j.ijhydene.2010.07.009>.
- [32] Norouzifard V, Bahrami M. Analytical Modeling of PEM Fuel Cell Gas Diffusion Layers Deformation under Compression: Part 2 - Nonlinear Behaviour Region. *ECS Trans* 2014;61:13. <https://doi.org/10.1149/06111.0013ecst>.
- [33] Chen Y, Zhao J, Jin C, Ke Y, Li D, Wang Z. Effect of Clamping Compression on the Mechanical Performance of a Carbon Paper Gas Diffusion Layer in Polymer Electrolyte Membrane Fuel Cells. *Membranes* 2022;12:645. <https://doi.org/10.3390/membranes12070645>.
- [34] Koorata PK, Bhat SD. Compressive cyclic response of PEM fuel cell gas diffusion media. *Int J Hydrog Energy* 2021;46:5570–9. <https://doi.org/10.1016/j.ijhydene.2020.11.023>.
- [35] Chen Y, Ke Y, Xia Y, Cho C. Investigation on Mechanical Properties of a Carbon Paper Gas Diffusion Layer through a 3-D Nonlinear and Orthotropic Constitutive Model. *Energies* 2021;14:6341. <https://doi.org/10.3390/en14196341>.
- [36] Ettouhami MK, Atifi A, Mounir H, Amadane Y. Numerical simulation of Effect of Contact Pressure on Mechanical Behavior of Gas Diffusion Layers (GDL) and PFSA

- [37] Serincan MF, Pasaogullari U. Effect of gas diffusion layer anisotropy on mechanical stresses in a polymer electrolyte membrane. *J Power Sources* 2011;196:1314–20. <https://doi.org/10.1016/j.jpowsour.2010.06.026>.
- [38] Zhou Y, Lin G, Shih AJ, Hu SJ. Multiphysics Modeling of Assembly Pressure Effects on Proton Exchange Membrane Fuel Cell Performance. *J Fuel Cell Sci Technol* 2009;6:041005. <https://doi.org/10.1115/1.3081426>.
- [39] Lee T, Yang C. A parametric study on the deformation of gas diffusion layer in PEM fuel cell. *J Mech Sci Technol* 2020;34:259–68. <https://doi.org/10.1007/s12206-019-1227-8>.
- [40] Gigos PA, Faydi Y, Meyer Y. Mechanical characterization and analytical modeling of gas diffusion layers under cyclic compression. *Int J Hydrog Energy* 2015;40:5958–65. <https://doi.org/10.1016/j.ijhydene.2015.02.136>.
- [41] Norouzifard V, Bahrami M. Deformation of PEM fuel cell gas diffusion layers under compressive loading: An analytical approach. *J Power Sources* 2014;264:92–9. <https://doi.org/10.1016/j.jpowsour.2014.04.057>.
- [42] Toll S. Packing mechanics of fiber reinforcements. *Polym Eng Sci* 1998;38:1337–50. <https://doi.org/10.1002/pen.10304>.
- [43] Van Wyk CM. 20—NOTE ON THE COMPRESSIBILITY OF WOOL. *J Text Inst Trans* 1946. <https://doi.org/10.1080/19447024608659279>.
- [44] Carral C, Mele P. Modeling the original and cyclic compression behavior of non-woven gas diffusion layers for fuel cells. *Int J Hydrog Energy* 2022;47. <https://doi.org/10.1016/j.ijhydene.2022.05.121>.
- [45] Hoppe E, Janßen H, Müller M, Lehnert W. The impact of flow field plate misalignment on the gas diffusion layer intrusion and performance of a high-temperature polymer electrolyte fuel cell. *J Power Sources* 2021;501:230036. <https://doi.org/10.1016/j.jpowsour.2021.230036>.
- [46] Khajeh-Hosseini-Dalasm N, Sasabe T, Tokumasu T, Pasaogullari U. Effects of polytetrafluoroethylene treatment and compression on gas diffusion layer microstructure using high-resolution X-ray computed tomography. *J Power Sources* 2014;266:213–21. <https://doi.org/10.1016/j.jpowsour.2014.05.004>.
- [47] Tötze C, Gaiselmann G, Osenberg M, Bohner J, Arlt T, Markötter H, et al. Three-dimensional study of compressed gas diffusion layers using synchrotron X-ray imaging. *J Power Sources* 2014;253:123–31. <https://doi.org/10.1016/j.jpowsour.2013.12.062>.
- [48] Castanheira L. DOLPHIN Workshop : Design and Modelling resized 2021.
- [49] Choi J, Cha Y, Kong J, Vaz N, Lee J, Ma S-B, et al. Multi-Variate Optimization of Polymer Electrolyte Membrane Fuel Cells in Consideration of Effects of GDL

- Compression and Intrusion. *J Electrochem Soc* 2022;169:014511. <https://doi.org/10.1149/1945-7111/ac492f>.
- [50] Wang X-D, Yan W-M, Duan Y-Y, Weng F-B, Jung G-B, Lee C-Y. Numerical study on channel size effect for proton exchange membrane fuel cell with serpentine flow field. *Energy Convers Manag* 2010;51:959–68. <https://doi.org/10.1016/j.enconman.2009.11.037>.
- [51] Lai Y-H, Li Y, Rock JA. A novel full-field experimental method to measure the local compressibility of gas diffusion media. *J Power Sources* 2010;195:3215–23. <https://doi.org/10.1016/j.jpowsour.2009.11.122>.
- [52] Xiao L, Luo M, Zhang H, Zeis R, Sui P-C. Solid Mechanics Simulation of Reconstructed Gas Diffusion Layers for PEMFCs. *J Electrochem Soc* 2019;166:F377–85. <https://doi.org/10.1149/2.0421906jes>.
- [53] Xiao L, Zhu L, Clökler C, Grünzweig A, Wilhelm F, Scholta J, et al. Experimental validation of pore-scale models for gas diffusion layers. *J Power Sources* 2022;536. <https://doi.org/10.1016/j.jpowsour.2022.231515>.
- [54] Xiao L, Yin Z, Bian M, Bevilacqua N, Zeis R, Yuan J, et al. Microstructure reconstruction using fiber tracking technique and pore-scale simulations of heterogeneous gas diffusion layer. *Int J Hydrog Energy* 2022;47:20218–31. <https://doi.org/10.1016/j.ijhydene.2022.04.143>.
- [55] Zhang Z, He P, Dai Y-J, Jin P-H, Tao W-Q. Study of the mechanical behavior of paper-type GDL in PEMFC based on microstructure morphology. *Int J Hydrog Energy* 2020;45:29379–94. <https://doi.org/10.1016/j.ijhydene.2020.07.240>.
- [56] Kandlikar SG, Lu Z, Lin TY, Cooke D, Daino M. Uneven gas diffusion layer intrusion in gas channel arrays of proton exchange membrane fuel cell and its effects on flow distribution. *J Power Sources* 2009;194:328–37. <https://doi.org/10.1016/j.jpowsour.2009.05.019>.
- [57] Nitta I, Hottinen T, Himanen O, Mikkola M. Inhomogeneous compression of PEMFC gas diffusion layer Part I. Experimental. *J Power Sources* 2007:11.
- [58] SGL Carbon. Datasheet - SGL Sigracet 22BB 2020. <https://www.sglcarbon.com/en/markets-solutions/material/sigracet-fuel-cell-components/>.
- [59] GORE. GORE® Fuel Cell Technologies 2023.
- [60] COMSOL Multiphysics® v. 6.0. Structural Mechanics Module User’s Guide. Stockholm, Sweden.: 2022.
- [61] Ouerghemmi M, Carral C, Mele P. Experimental study of gas diffusion layers nonlinear orthotropic behavior. In: Cigolotti V, editor. E3S Web Conf., vol. 334, 2022, p. 04020. <https://doi.org/10.1051/e3sconf/202233404020>.

- [62] Mezeix L, Bouvet C, Huez J, Poquillon D. Mechanical behavior of entangled fibers and entangled cross-linked fibers during compression. *J Mater Sci* 2009;44:3652–61. <https://doi.org/10.1007/s10853-009-3483-y>.
- [63] Tötze C, Gaiselmann G, Osenberg M, Arlt T, Markötter H, Hilger A, et al. Influence of hydrophobic treatment on the structure of compressed gas diffusion layers. *J Power Sources* 2016;324:625–36. <https://doi.org/10.1016/j.jpowsour.2016.05.118>.
- [64] Sadeghifar H, Djilali N, Bahrami M. Effect of Polytetrafluoroethylene (PTFE) and micro porous layer (MPL) on thermal conductivity of fuel cell gas diffusion layers: Modeling and experiments. *J Power Sources* 2014;248:632–41. <https://doi.org/10.1016/j.jpowsour.2013.09.136>.
- [65] Afrasiab H, Davoodi KH, Barzegari MM, Gholami M, Hassani A. A novel constitutive stress-strain law for compressive deformation of the gas diffusion layer. *Int J Hydrog Energy* 2022. <https://doi.org/10.1016/j.ijhydene.2022.07.127>.
- [66] Carral C, Mele P. A numerical analysis of PEMFC stack assembly through a 3D finite element model. *Int J Hydrog Energy* 2014;39:4516–30. <https://doi.org/10.1016/j.ijhydene.2014.01.036>.
- [67] Chippar P, O K, Kang K, Ju H. A numerical investigation of the effects of GDL compression and intrusion in polymer electrolyte fuel cells (PEFCs). *Int J Hydrog Energy* 2012;37:6326–38. <https://doi.org/10.1016/j.ijhydene.2011.04.154>.
- [68] Movahedi M, Ramiar A, Ranjber AA. 3D numerical investigation of clamping pressure effect on the performance of proton exchange membrane fuel cell with interdigitated flow field. *Energy* 2018;142:617–32. <https://doi.org/10.1016/j.energy.2017.10.020>.
- [69] Belgacem N, Pauchet J, Prat M. On the current distribution at the channel – rib scale in polymer-electrolyte fuel cells. *Int J Hydrog Energy* 2018;43:5112–23. <https://doi.org/10.1016/j.ijhydene.2018.01.097>.
- [70] Hottinen T, Himanen O, Karvonen S, Nitta I. Inhomogeneous compression of PEMFC gas diffusion layer: Part II. Modeling the effect. *J Power Sources* 2007;171:113–21. <https://doi.org/10.1016/j.jpowsour.2006.10.076>.
- [71] Randrianarizafy B, Schott P, Chandesris M, Gerard M, Bultel Y. Design optimization of rib/channel patterns in a PEMFC through performance heterogeneities modelling. *Int J Hydrog Energy* 2018;43:8907–26. <https://doi.org/10.1016/j.ijhydene.2018.03.036>.
- [72] Asghari S, Mokmeli A, Samavati M. Study of PEM fuel cell performance by electrochemical impedance spectroscopy. *Int J Hydrog Energy* 2010;35:9283–90. <https://doi.org/10.1016/j.ijhydene.2010.03.069>.